Supporting Information

Design of Grid-Like Triple-Carbon Matrix Confined Ultrafine CoTe₂ Nanocrystals Toward Durable and Fast Potassium Storage

Zhijiao Huang,[a] Shiyun Xiong,[a] Wei Zhang,[a,*] Gaoyu Wang,[a] Lixiang Wang,[b] Jian Peng,[c] Qinghua Li,[a] Zhixin Liang,[a] Yajuan Cheng,[d,*] Shaoming Huang[a,*]

[a] *School of Materials and Energy. Guangzhou Key Laboratory of Low-Dimensional Materials and Energy Storage Devices. Guangdong University of Technology. Guangzhou 510006, China. E-mail: zhwei@gdut.edu.cn; smhuang@gdut.edu.cn*

[b] *School of Mechanical and Electrical Engineering. Jiaxing Nanhu University. Zhejiang 314001, China*

[c] *Institute for Superconducting and Electronic Materials Australian Institute for Innovative Materials University of Wollongong Innovation Campus Squires Way North Wollongong, NSW 2522, Australia*

[d] *School of Physics and Materials Science, Guangzhou University, Guangzhou 510006, China. E-mail: yajuancheng@gzhu.edu.cn*

Author Contributions

Z. H. and S. X. contributed equally to this work.

SectionI. Experimental Section

Synthesis of ZIF-67： In this experiment, 1.746 g of $Co(NO_3)_2 \cdot 6H_2O$ and 2.955 g of 2-methylimidazole were separately dissolved into 60 mL of methanol (AR) solution. The methanol solution of $Co(NO_3)_2 \cdot 6H_2O$ was then rapidly poured into the methanol solution of 2-methylimidazole, followed by vigorous stirring for 5 min. The mixture was then left to stand for 24 hours, after which the precipitate was collected and washed three times with methanol through centrifugation. Finally, the sample was dried 12 h in a vacuum oven at 70 ^{o}C.

Synthesis of Co@D-NC： The prepared ZIF-67 was placed in a tubular furnace for carbonization. The temperature was increased at a rate of 5 ^{o}C/min under an argon atmosphere until reaching 450 ^{o}C, and then maintained for 2 hours. PDA Coating: 80 mg of carbonized ZIF-67 (Co_3O_4@NC) was dispersed in an 80 mL ethanol solution containing 193.8 mg of trimethylolpropane, followed by thorough stirring. Subsequently, 80 mg of dopamine hydrochloride was added, and the mixture was stirred for 24 hours. The product was then collected by centrifugation after washing six times with ethanol, which ensures the removal of Fe as evidenced by our Inductively Coupled Plasma-mass Spectrometry (ICP) analysis (Table S11). The washed sample was then subjected to another round of carbonization, with the temperature being increased at a rate of 5 ^{o}C/min under an argon atmosphere until reaching 500 ^{o}C, and it was maintained for 2 hours at 500 ^{o}C. This process resulted in the formation of Co@D-NC.

Synthesis of CoTe$_2$@T-NC and CoTe$_2$@D-NC: PPy Coating: 10 mg of sodium dodecylbenzene sulfonate was dissolved in 10 mL of deionized water. Afterward, 40 mg of Co@D-NC was added to this solution and stirred thoroughly to ensure a uniform mixture. Next, 10 mL of a pyrrole solution, containing 30 μL of pyrrole, was added and stirred for 30 minutes. Following this, 10 mL of $FeCl_3$ solution (0.2 M) was added, and the mixture was stirred for 2 hours in an ice bath. The resultant sample was collected via centrifugation, washed six times with deionized water and ethanol, and then dried overnight in a vacuum oven at 70°C. The dried sample was subjected

to high-temperature *in-situ* tellurization by increasing the temperature at a rate of 2 °C /min under an argon atmosphere until reaching 550 °C, and then maintained at 550 °C for 5 hours. This process resulted in the formation of $CoTe_2$@T-NC. $CoTe_2$@D-NC was obtained by *in-situ* high-temperature tellurization of sample (one layer of PPy coating) under the same conditions as the synthesis of $CoTe_2$@D-NC.

Synthesis of $CoTe_2$@NC： $CoTe_2$@NC was obtained through *in-situ* tellurization of carbonized ZIF-67 using the same method as the synthesis of $CoTe_2$@T-NC.

Materials Characterization: The microstructures and morphologies of the samples were characterized through field-emission scanning electron microscopy (FESEM, Thermo Fisher Scientific Apreo C, USA) and transmission electron microscopy (TEM, Talos F200S, FEI, Thermo). The phase variations during charge/discharge processes were characterized by X-ray diffraction (XRD, SmartLab9KW with Cu-Kα radiation at 40 kV, λ = 1.541 Å), Raman spectroscopy (Renishaw InVia, 532 nm excitation wavelength) and energy-dispersive spectroscopy (EDS, FEI Talos F200S), X-ray photoelectron spectroscopy (XPS, Escalab 250Xi). The carbon content in $CoTe_2$@T-NC was examined by thermogravimetric analysis (TGA DSC 3+, Mettler Toledo) at a heating rate of 10 °C min^{-1} under air atmosphere. Ultraviolet-visible (UV–vis) absorption spectra of $CoTe_2$@NC, $CoTe_2$@D-NC and $CoTe_2$@T-NC anodes were collected during the initial fully discharged state at 0.02 A g^{-1} by using a UV-2600 spectrophotometer with a sampling interval of 0.2 nm.

Electrochemical Measurements： In an inert atmosphere (Ar), button cells (type 2032) were assembled for the electrochemical characterization of $CoTe_2$@T-NC electrodes. The $CoTe_2$@T-NC electrode was prepared by uniformly mixing the active material $CoTe_2$@T-NC (80 wt%), a conductive agent (graphene, 10 wt%), a binder consisting of sodium carboxymethyl cellulose (5 wt%) and polybutadiene rubber (5 wt%), and deionized water, and then coating the mixture onto a copper foil. The coated electrode was subsequently dried in a vacuum oven at 70 °C. The loading mass of the anode is approximately 1 mg/cm^2, and the cathode loading mass is about 3 mg/cm^2. In the half-cell configuration, a Potassium tablet was used as the counter

electrode, and a glass fiber separator (Whatman GF/D, thickness of 0.657 mm) was employed. The electrolyte consisted of a 3 M solution of potassium bis (fluorosulfonyl)imide (KFSI) in ethylene glycol dimethyl ether. All the values of specific capacity were calculated based on the mass of $CoTe_2$@T-NC. CV measurements were performed on an Autolab instrument (PGSTAT 302) at a scanning rate of 0.1 mV s^{-1}. Electrochemical impedance spectroscopy (EIS) measurements were carried out using an Autolab 302N electrochemical workstation, covering a frequency range from 10^5 to 0.1 Hz at an amplitude of 5 mV. The in-situ EIS tests were meticulously performed after assembling the coin-type cell, with measurements recorded at various potentials and at a current density of 0.1 A g^{-1}

The galvanostatic charge/discharge tests were conducted on a Neware battery test system (CT-ZWJ-4'S-T-1U, Shenzhen, China). In the electrolytic cell of *in-situ* UV-visible, the working electrodes were prepared by mixing 80 wt% of the active materials, 10 wt% of polyvinylidene fluoride (PVDF) and 10 wt% of graphene (GN) with N-methyl-2-pyrrolidone (NMP) as the solvent. The slurry was uniformly coated onto an Al foil and dried at 70 °C for 12 h under a vacuum. K metal and 3 M KFSI in DME were used as the counter electrode and the electrolyte, respectively. GITT tests were conducted by discharging and charging the cells at 0.02 A g^{-1} for 30 min with a rest interval of 2 h in the range of 0.01 to 3.0 V.

DFT Calculations: The Vienna Ab initio Simulation Package (VASP)[1] was employed to perform all density functional theory (DFT) calculations within the generalized gradient approximation (GGA) using the Perdew-Burke-Ernzerhof (PBE) functional and the projected augmented wave (PAW) pseudopotential.[2-3] A kinetic energy cut-off of 500 eV was used for the plane-wave basis set. The DFT-D3 empirical correction method was employed to describe van der Waals interactions.[4] Geometry optimizations were performed with a force tolerance of 0.05 eV/Å. The models of K_2Te_3 and K_5Te_3 clusters were extracted from the corresponding crystal structures to represent the nanoparticles in our experiment. For the structural model of the carbon substrate, perfect and defective graphene was employed to explore the interactions between substrates and K_2Te_3/ K_5Te_3 clusters .[5,6] A supercell of 7 × 7 unit

cells for graphene was adopted in all DFT calculations. The size of the K_2Te_3 and K_5Te_3 are approximately $5.1 \times 4.4 \times 2.1$ and $6.37 \times 6.49 \times 3.98$ Å, respectively. A vacuum height of 15 Å angstrom was used to mimic the 2-dimensional systems. Due to the large supercell being adopted, a Monkhorst-Pack k-grid of $1 \times 1 \times 1$ was applied for all the calculations. The adsorption energy (E_a) was calculated by the equation: $E_a = E_{(slab + KxTey)} - E_{(slab)} - E_{(KxTey)}$. Where $E_{(slab + KxTey)}$ and $E_{(slab)}$ are the total energy of the surface slab with and without K_xTe_y, respectively, and $E_{(KxTey)}$ is the total energy of the K_xTe_y clusters.

Calculation of the $CoTe_2$ content in $CoTe_2@T-NC$ from TGA analysis:

The $CoTe_2$ content in $CoTe_2@T-NC$ was determined through thermogravimetric analysis (TGA). The $CoTe_2$ content was calculated based on the mass loss from carbon combustion (Fig. S4a) and the increased mass due to the oxidation of $CoTe_2$ to $Co_2Te_3O_8$ ($2CoTe_2 + 5O_2 + C \rightarrow Co_2Te_3O_8 + Te\uparrow + CO_2\uparrow$, Fig. S4b). The literature confirms that Te volatilizes as a gas at temperatures up to 700°C during TGA analysis. [7,8] Furthermore, the XRD results show only diffraction signals of $Co_2Te_3O_8$, with no indication of the presence of Te (Reaction equation: $2CoTe_2 + 5O_2 + C \rightarrow Co_2Te_3O_8 + Te\uparrow + CO_2\uparrow$).

Based on the above results, the procedure for calculating the $CoTe_2$ content in $CoTe_2@T-NC$ composites are described as follows:

$$CoTe_2(wt\%) = Co_2Te_3O_8(wt\%) \times 2 \times \frac{M(CoTe_2)}{M(Co_2Te_3O_8)}$$

$$= Co_2Te_3O_8(wt\%) \times 2 \times \frac{314.1}{628.8}$$

$$\approx Co_2Te_3O_8(wt\%)$$

Where, the $M(CoTe_2)$ and $M(Co_2Te_3O_8)$ represent the relative molecular weights of $CoTe_2$ and $Co_2Te_3O_8$, respectively. We have also indicated in the TGA that Te exists in a gaseous form. Finally, the $CoTe_2$ mass fraction in $CoTe_2@T-NC$ was calculated

to be 60.0% using the formula.

Evaluation of capacitance effect and the calculation of pseudocapacitive contribution:

The capacitance effect can be determined from the CV curve by measuring the peak current (i) and the scan rate (v), as shown below.

$$i = a\, v^b,$$

$$\log i = b \log v + \log a$$

Whereas a and b are fitting parameters, i and v represent the peak current and scan rate, respectively. The capacitance behavior can be estimated using the b-value, which is the slope of the "$\log i$ *vs.* $\log v$" plot .[9] For diffusion-controlled behavior, the b-value approaches 0.5, while for processes dominated by surface capacitance, it approaches 1.0.[10,11] Additionally, the pseudocapacitive contribution can also be calculated using the following equation:

$$i = k_1\, v + k_2\, v^{1/2},$$

Where $k_1 v$ and $k_2 v^{1/2}$ represent the pseudocapacitive contribution and ion diffusion contribution, respectively.

Calculation of the diffusion coefficient (DK$^+$):

The galvanostatic intermittent titration technique (GITT) test was conducted by discharging or charging the battery at a constant current of 20 mA g^{-1} for 30 minutes, followed by a 2 h rest period within the voltage range of 0.01 to 3.0 V. The diffusion coefficient can be worked out by solving Fick's second law:

$$D = \frac{4}{\pi\tau}\left(\frac{M_B V_M}{M_B S}\right)^2 \left(\frac{\Delta E_s}{\Delta E_\tau}\right)^2 \left(\tau \ll \frac{L^2}{D}\right)$$

Where τ is the duration of the current pulse (s), m_B, V_M, M_B, and S represent the mass, molar volume, molar mass, and electrode area of the active material, respectively. ΔE_S denotes the quasi-thermodynamic equilibrium potential difference between the pre- and post-current pulse, while ΔE_τ refers to the potential difference during the current pulse .[10]

Calculation of power density and energy density:

The energy density (E, Wh kg^{-1}) and power density (P, W kg^{-1}) of the hybrid

capacitor were calculated using the following formulas:

$$E = \frac{VIt}{m} \qquad P = \frac{VI}{m} \qquad \Delta V = \frac{(V_{max} + V_{min})}{2}$$

where I is the discharge current, t the discharge cycle duration, V_{max} and V_{min} represent the initial and final voltages after removing the voltage drop during discharge, and m is the total mass of active material in both the cathode and anode. The loading mass of the anode is approximately 1 mg/cm^2, while that of the cathode is about 3 mg/cm^2.

Section II. Supplementary Figures and Tables
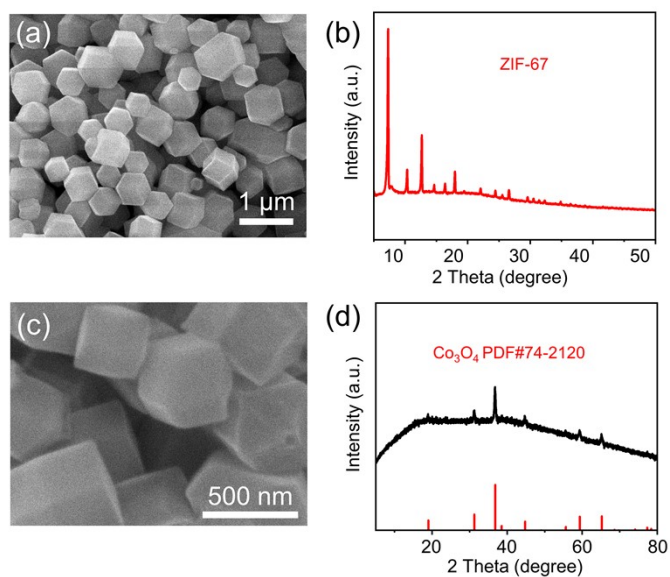
Fig. S1 (a) SEM image, (b) XRD patterns of ZIF-67. (c) SEM image, (d) XRD patterns of carbonized MOF (Co_3O_4@NC).

The Co_3O_4@NC composites exhibit a uniform polyhedral structure (**Fig.** S1c), albeit with a notably smaller diameter compared to the original MOF precursor (**Fig.** S1a). The X-ray diffraction (XRD) analysis, as shown in **Fig.** S1c, reveals that all characteristic peaks align well with the standard pattern of cubic crystalline Co_3O_4 (JCPDS No. 74-2120).
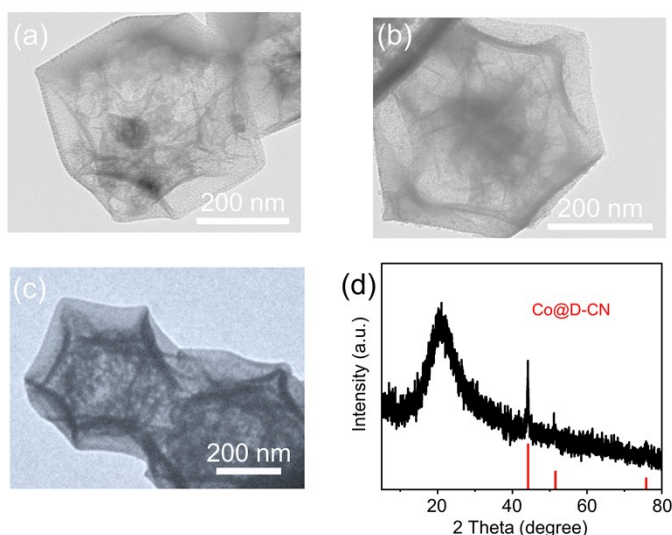
Fig. S2 TEM images of different precursors after high-temperature carbonization: (a) ZIF-67, PDA- coated Co_3O_4@NC for (b) 12 h and (c) 24 h. (d) XRD patterns of sample coated with PDA and carbonized (Co@D-NC).

To substantiate the formation of an interwoven PDA-derived carbon grid within the polyhedral structure, we conducted a comparative TEM analysis of the composites before and after polymerization of dopamine hydrochloride. Fig. S2b and c display the TEM results post-polymerization for 12 and 24 h, followed by high-temperature carbonization, respectively. A comparison with Fig. S2a clearly shows the formation of a grid-like carbon matrix inside the polyhedron in Fig. S2b. Notably, there is no significant increase in wall thickness, suggesting that dopamine hydrochloride molecules predominantly infiltrate the fluffy polyhedral structure through capillary action, initiating polymerization along the inner ultrathin carbon layer. With prolonged polymerization time, the grid-like carbon layer becomes more compact, accompanied by a small amount of surface polymerization.
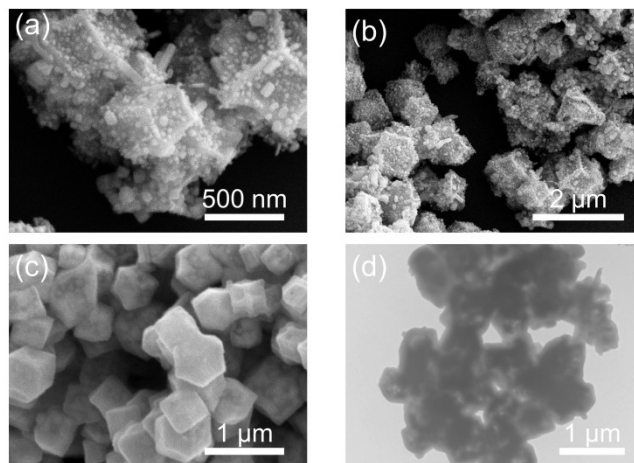
Fig. S3 SEM images of (a and b) CoTe$_2$@NC with differing magnifications. (c) SEM image and (d) TEM image of CoTe$_2$@D-NC.

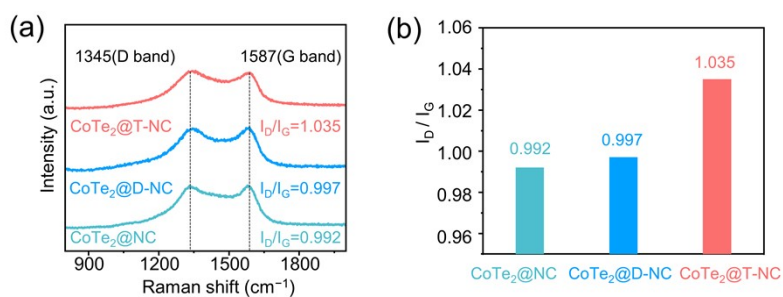**Fig. S4** (a) Raman spectra and (b) bar statistical plot of I$_D$/I$_G$ values of CoTe$_2$@T-NC, CoTe$_2$@D-NC, and CoTe$_2$@NC.
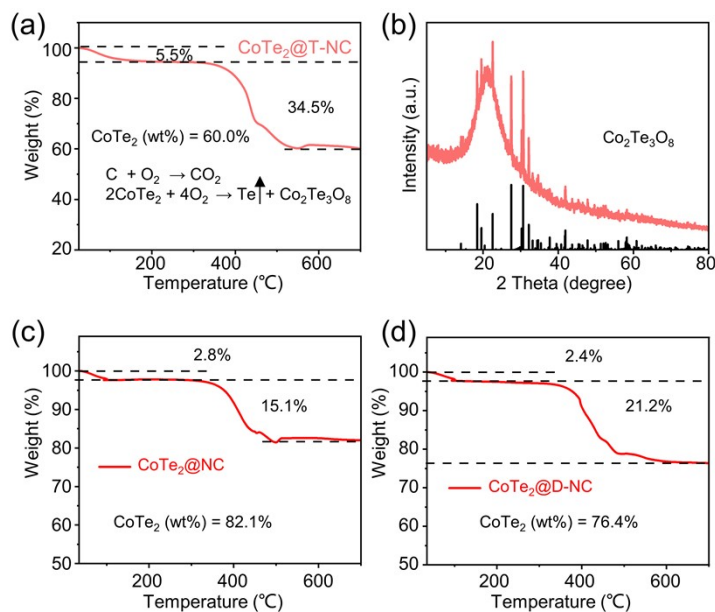
Fig. S5 Thermogravimetric analysis (TGA) curves of (a) CoTe$_2$@T-NC, (c) CoTe$_2$@D-NC, and (d) CoTe$_2$@NC. (b) XRD pattern of the CoTe$_2$ oxidation product.

The TGA test results reveal that the carbon content in CoTe$_2$@NC and CoTe$_2$@D-NC samples is 15.1% and 21.2%, respectively. With the previously established carbon content of 34.5% in CoTe$_2$@T-NC, we estimate that the PDA-derived and PPy-derived carbon contents are approximately 16.9% and 6.0%, respectively.
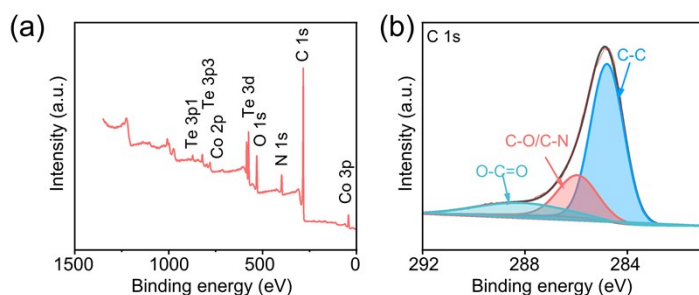

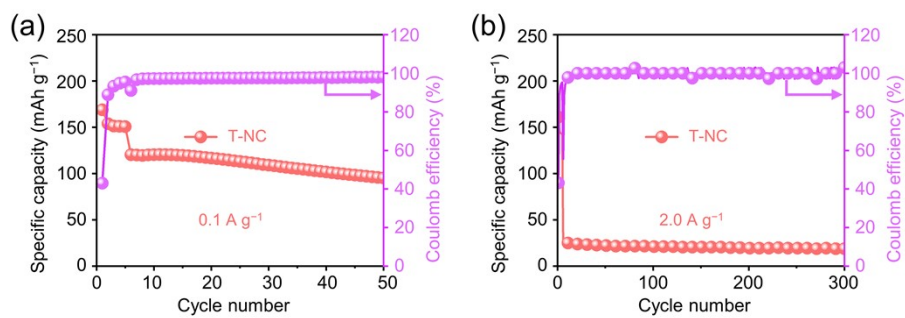**Fig. S6** (a) XPS survey spectrum, and (b) XPS high-resolution spectra of C 1s of CoTe$_2$@T-NC.

Fig. S7 Cycling performance of N-doped pyrolytic carbon (T-NC) in $CoTe_2$@T-NC at a current density of (a) 0.1 A g^{-1} and (b) 2.0 A g^{-1}
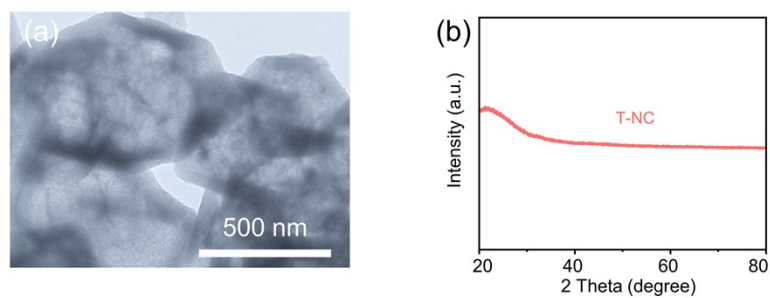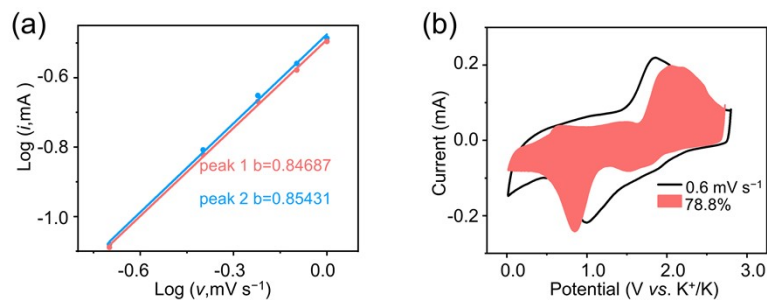

Fig. S8 (a) SEM image, (b) XRD patterns of T-NC.

Fig. S9 (a) The relationship between log i and log v of CoTe$_2$@T-NC electrode, where i is the peak current, v is the scanning rate, and b is the slope of log (i) vs. log (v). (b) Capacity contribution at a scanning rate of 0.6 mV s^{-1}.
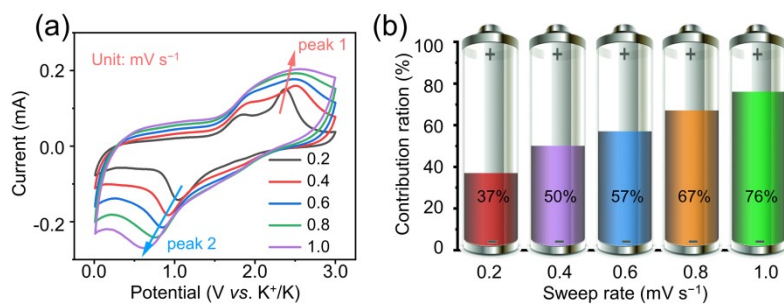
Fig. S10 (a) CV curves at various scan rates, (b) contribution ratios of capacitive-controlled capacity of CoTe$_2$@D-NC electrode.
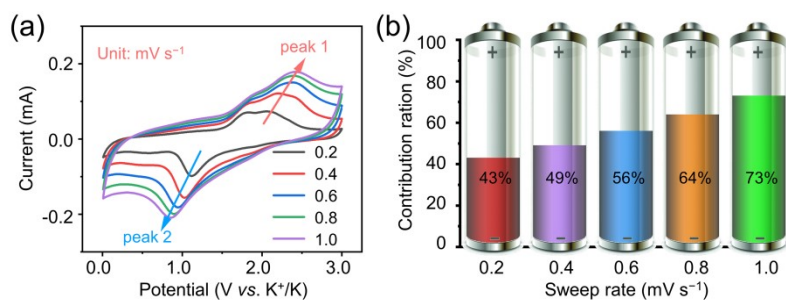
Fig. S11 (a) CV curves at various scan rates, (b) contribution ratios of capacitive-controlled capacity of CoTe$_2$@NC.
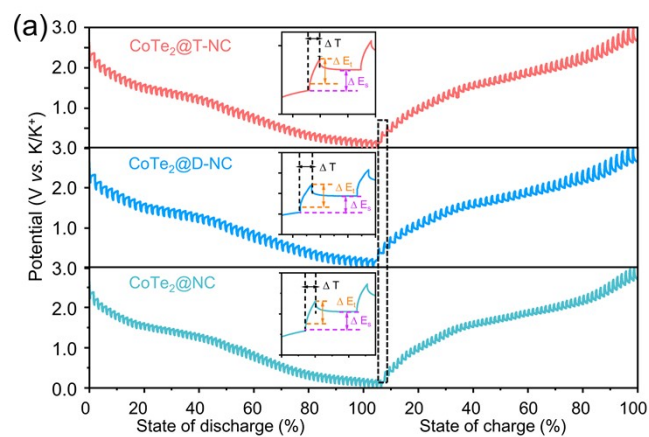
Fig. S12 (a) galvanostatic intermittent titration technique (GITT) curves of CoTe$_2$@T-NC, CoTe$_2$@D-NC, and CoTe$_2$@NC.

CoTe$_2$@T-NC anode

Metal K cathode

Electrolyte (3M KFSI in DME)
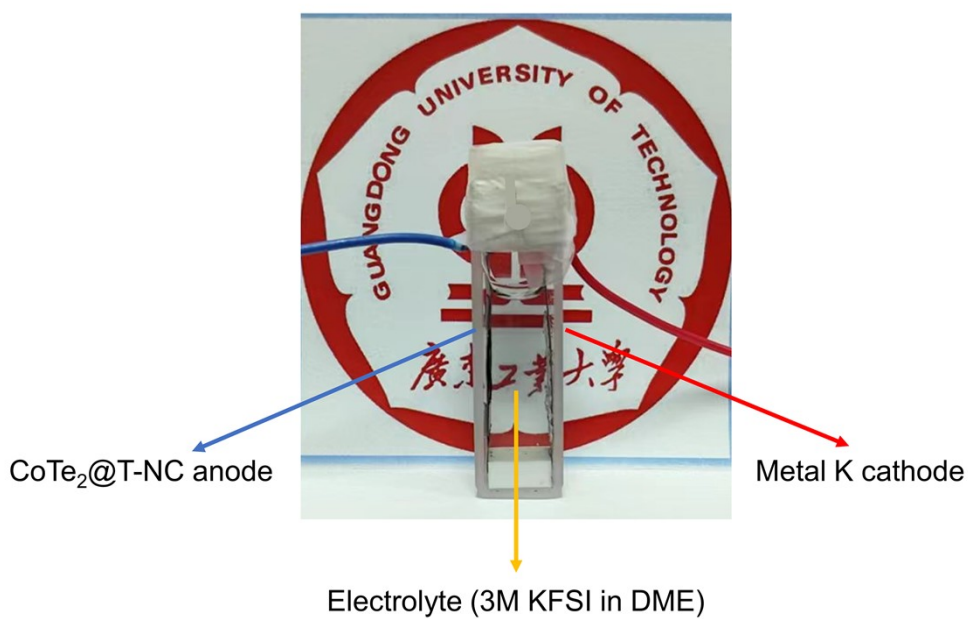
Fig. S13 The electrolytic cell for the collection of *in-situ* UV-vis absorption spectra.
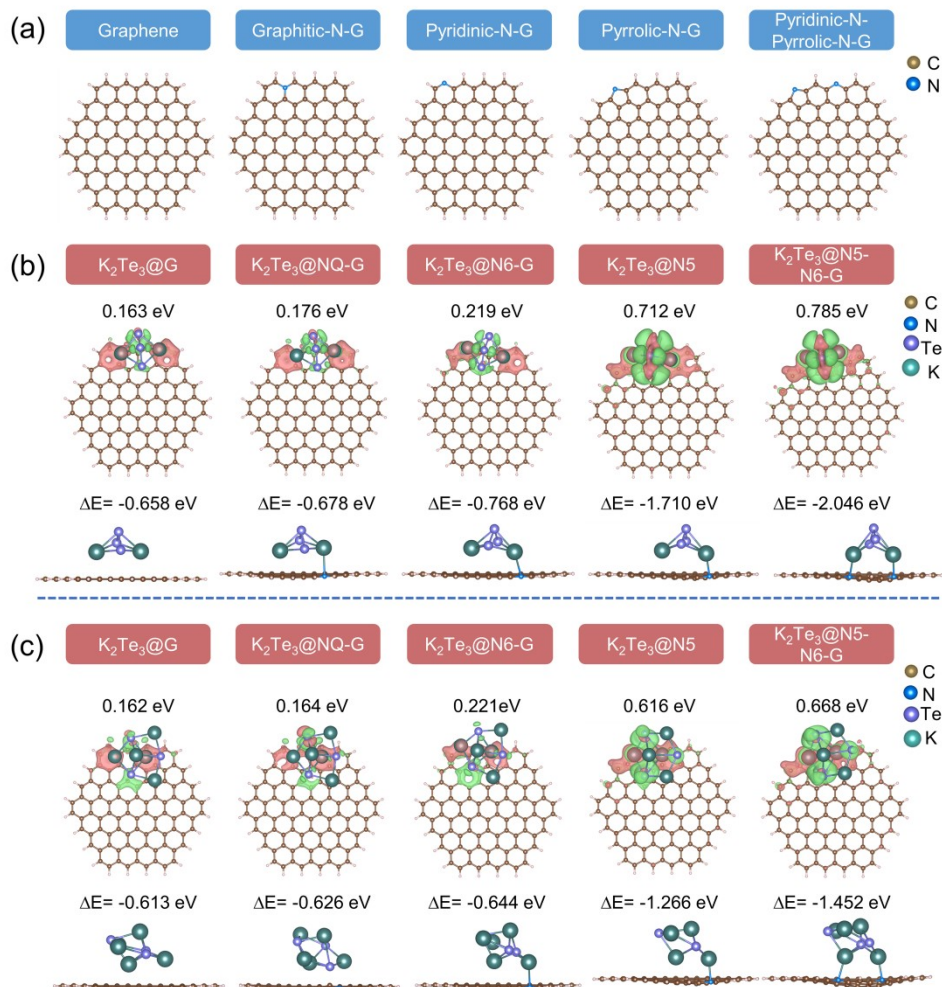
Fig. S14 (a) top view of carbon structures of graphene, graphene-N, pyridine-N, pyrrole-N, and pyridine pyrrole-N disks. Top views of electron density differences and side views of corresponding structures for (b) K_2Te_3 and (c) K_5Te_3 adsorbed on graphene, graphene-N, pyridine-N, pyrrole-N, and pyridine pyrrole-N disks.
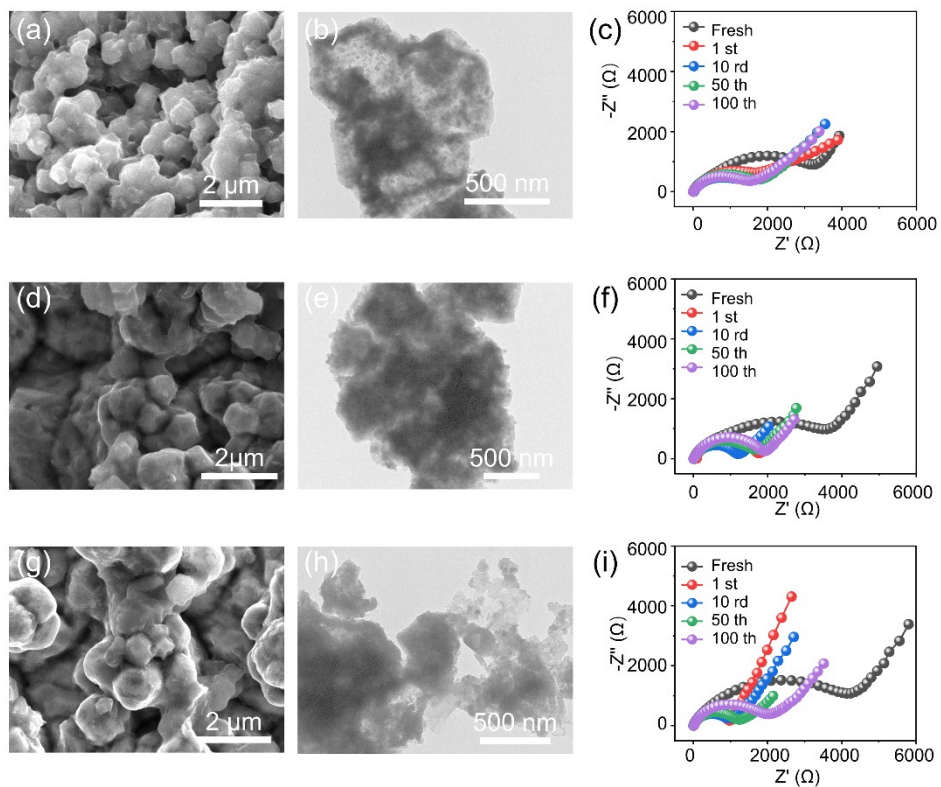
Fig. S15 SEM (a) and TEM (b) images of CoTe$_2$@T-NC electrode, SEM (d) and TEM (e) images of CoTe$_2$@D-NC electrode, SEM (g) and TEM (h) images of CoTe$_2$@NC electrode after 100 cycles at 1.0 A g^{-1}, respectively. EIS curves of (c) CoTe$_2$@T-NC electrode, (f) CoTe$_2$@D-NC electrode, (i) of CoTe$_2$@NC after 100 cycles at 1.0 A g^{-1}
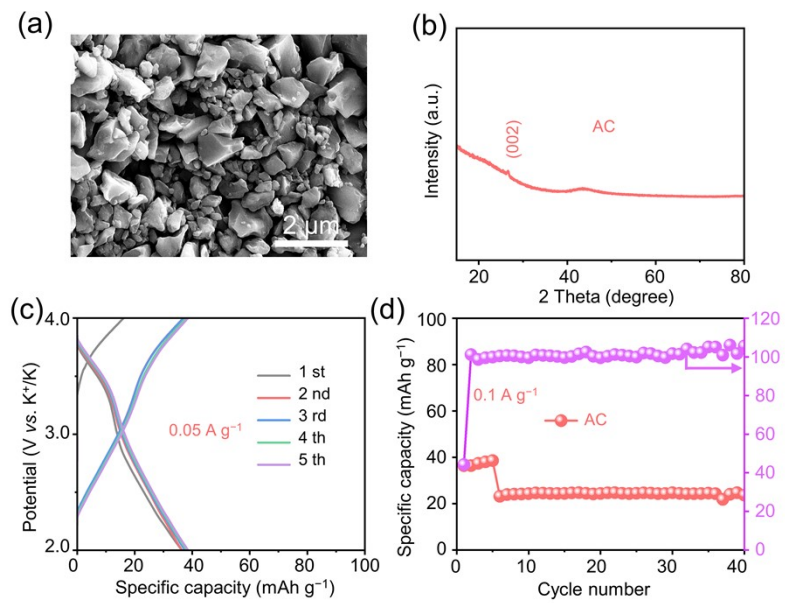
Fig. S16 (a) SEM image, (b) XRD patterns, (c) first five charge–discharge profiles, (d) cycling performance of CoTe$_2$@T-NC at 0.1 A g^{-1} of AC.

Table S1. The density of typical transition metal tellurides

Materials	CoTe$_2$	ZnTe	CoSe$_2$	ZnSe	CoS$_2$	ZnS
Density (g cm^{-3})	8.05	6.34	7.16	5.90	4.82	4.08

Table S2. Atomic contents of pyridinic-N (N-6), pyrrolic-N (N-5), and graphitic-N (N-Q)

Nitrogen type	N-Q	N-6	N-5
Atomic content (%)	16.1	40.1	43.8

Table S3. The contributed reversible capacity of each component (CoTe$_2$ and C) in the CoTe$_2$@T-NC composite.

Current density (A g^{-1})	Cycle number	CoTe$_2$@T-NC (mAh g^{-1})	T-NC (mAh g^{-1})	Ratio (T-NC / CoTe$_2$@T-NC)
0.1	50	340.0	95.3	9.6%
2.0	300	247.8	18.9	2.6%

The specific capacities of N-doped porous carbon (T-NC) in CoTe$_2$@T-NC are about 95.3 and 18.9 mAh g^{-1} after 50 and 300 cycles at 0.1 and 2.0 A g^{-1}, respectively. Based on the charging-specific capacity and the carbon content, the capacity contribution of T-NC in the CoTe$_2$@T-NC composite was calculated. In detail, the capacity contribution ratio of T-NC in the CoTe$_2$@T-NC composite is 9.6% ($\frac{95.3 \times 34.5\%}{340.0} \approx 9.6\%$) at 0.1 A g^{-1} and 2.6% ($\frac{18.9 \times 34.5\%}{247.8} \approx 2.6\%$) at 2.0 A g^{-1}, respectively.

Table S4. Potassium storage performance comparison between the designed CoTe$_2$@T-NC electrode and other reported chalcogenides electrodes.

Active materials	Rate capability	Cyclic stability	Ref
CoTe$_2$@T-NC	213 mAh g^{-1}	1500 cycles at 2.0 A g^{-1}	This work
CoTe$_2$@NPCNFs @NC	120 mAh g^{-1}	1000 cycles at 2.0 A g^{-1}	S23
WS$_2$	48.2 mAh g^{-1}	400 cycles at 0.5A g^{-1}	S22
NCNF@CoSe$_2$	173 mAh g^{-1}	600 cycles at 2.0 A g^{-1}	S21
MoSe$_2$/C	226 mAh g^{-1}	1000 cycles at 1.0 A g^{-1}	S20
MoSe$_2$/MXene@ C	243 mAh g^{-1}	300 cycles at 2.0 A g^{-1}	S19
NiS$_2$@C@C	302.7 mAh g^{-1}	100cycles at 0.05A g^{-1}	S18
WTe$_2$	120mAh g^{-1}	50cycles at 0.1A g^{-1}	S17
MoS$_2$/C@NDG	220.7 mAh g^{-1}	150cycles at 1.0A g^{-1}	S16
v-MoSSe@CM	220.5 mAh g^{-1}	1000cycles at 0.5A g^{-1}	S15
ZnSeNP@NHC	132.9 mAh g^{-1}	1200cycles at 0.1A g^{-1}	S14
Sb$_2$Se$_3$@C	191.4 mAh g^{-1}	400cycles at 0.5A g^{-1}	S13
E-MoS$_2$/NOC TC	176 mAh g^{-1}	500cycles at1.0 A g^{-1}	S12

Table S5. EIS curve fitting impedance of CoTe$_2$@T-NC electrode discharged to different voltages

CoTe$_2$@T-NC	R_s ( )	R_{ct} ( )
Fresh	3.428	3787
D-2.5 V	4.122	4451
D-2.3 V	3.361	1851
D-2.0 V	7.132	4635
D-1.8 V	5.263	4806
D-1.5 V	4.569	6809
D-1.1 V	3.859	7107
D-0.8 V	4.039	6661
D-0.6 V	4.447	6364
D-0.01 V	4.272	7253

Table S6. EIS curve fitting impedance of CoTe$_2$@T-NC electrode charged to different voltages

CoTe$_2$@D-NC	R_s ( )	R_{ct} ( )
C-0.3 V	4.814	7186
C-0.6 V	4.267	5825
C-0.9 V	4.861	4180
C-1.4 V	5.717	3710
C-1.6 V	5.376	3591
C-1.8 V	5.465	4547
C-2.1 V	5.324	2703
C-2.4 V	4.548	2655
C-2.7 V	3.450	2110
C-3.0 V	5.486	2083

Table S7. Impedance of CoTe$_2$@T-NC electrodes with different number of cycles at a current density of 1 A g^{-1}

CoTe$_2$@T-NC	R_s ( )	R_{ct} ( )
Before cycling	3.41	3715
After 1 cycle	5.48	2105
After 10 cycles	4.88	1851
After 50 cycles	4.26	1784
After 100 cycles	4.15	1758

Table S8. Impedance of CoTe$_2$@D-NC electrode after different number of cycles at a current density of 1 A g^{-1}

CoTe$_2$@D-NC	R_s ( )	R_{ct} ( )
Before cycling	3.52	4255
After 1 cycle	63.30	1719
After 10 cycles	22.60	1231
After 50 cycles	30.40	1683
After 100 cycles	25.06	1934

Table S9. Impedance of CoTe$_2$@NC electrodes with different number of cycles at a current density of 1 A g^{-1}

CoTe$_2$@NC	R_s ( )	R_{ct} ( )
Before cycling	3.48	4638
After 1 cycle	13.46	1048
After 10 cycles	13.14	1124
After 50 cycles	16.75	1017

After 100 cycles	9.92	1340

Table S10. Comparison of performance between the designed potassium ion hybrid capacitor and the recently reported potassium ion capacitors

materials	power density (W kg^{-1})	energy density (Wh kg^{-1})	Ref
CoTe$_2$@T-NC//AC	863.62	116.6	This work
	2159.89	68.5	
	3460.53	51.0	
	4323.23	44.6	
	8654.36	24.9	
	12968.59	19.8	
K$_2$TP//AC	46	101	S27
	90	91	
	210	82	
	420	70	
	1100	61	
	2160	52	
BSH//AC	188	94	S26
	355	65	
	500	39	
	599	13.3	
	536	4.32	
3DTi$_3$C$_2$Tx//HPAC	121	98.4	S25
	220	92	
	500	78	
	1300	71	
	2200	49	
	4100	22	
	7016	18.7	
Co$_2$P@rGO-14//AC	12	87	S24
	20	60	
	60	55	
	200	45	
	350	40	
	700	32	
	1050	22	
	2100	15	
	4265	10	

Table S11. ICP testing of $CoTe_2$@T-NC.

Test Elements	Sample element content W (%)
Co	20.8147%
Fe	0.0000%

References:

1 K. G. and F. l. J., Phys. Rev. B, 1996, 54, 11169-11186.

2 P. J. P., B. Kieron and E. Matthias, Phys. Rev. Lett., 1996, 77, 3865-3868.

3 K. G. and J. D., Phys. Rev. B, 1999, 59, 1758-1775.

4 G. Stefan, A. Jens, E. Stephan and K. Helge, 2010, 132, 154104.

5 Q. Li, Y. Song, R. Xu, L. Zhang, J. Gao, Z. Xia, Z. Tian, N. Wei, M. H. Rümmeli, X. Zou, J. Sun and Z. Liu, *ACS Nano*, 2018, **12**, 10240–10250.

6 W. Yang, J. Zhou, S. Wang, Z. Wang, F. Lv, W. Zhang, W. Zhang, Q. Sun and S. Guo, *ACS Energy Lett.*, 2020, **5**, 1653–1661.

7 S. Yang, G. D. Park and Y. C. Kang, *Appl. Surf. Sci.*, 2020, **529**, 147140.

8 W. Zhang, X. Wang, K. W. Wong, W. Zhang, T. Chen, W. Zhao and S. Huang, *ACS Appl. Mater. Interfaces*, 2021, **13**, 34134–34144.

9 W. Zhao, W. Zhang, Y. Lei, L. Wang, G. Wang, J. Wu, W. Fan and S. Huang, *ACS Appl. Mater. Interfaces*, 2022, **14**, 6801–6809.

10 Q. Li, W. Zhang, J. Peng, D. Yu, Z. Liang, W. Zhang, J. Wu, G. Wang, H. Li and S. Huang, *Adv. Funct. Mater.*, 2022, **32**, 2112776.

11 Q. Li, W. Zhang, J. Peng, W. Zhang, Z. Liang, J. Wu, J. Feng, H. Li and S. Huang, *ACS Nano*, 2021, **15**, 15104–15113.

12 N. Zheng, G. Jiang, X. Chen, J. Mao, Y. Zhou and Y. Li, *J. Mater. Chem. A*, 2019, **7**, 9305–9315.

13 Z. Yi, Y. Qian, J. Tian, K. Shen, N. Lin and Y. Qian, *J. Mater. Chem. A*, 2019, **7**, 12283–12291.

14 Y. He, L. Wang, C. Dong, C. Li, X. Ding, Y. Qian and L. Xu, *Energy Storage Mater.*, 2019, **23**, 35–45.

15 Z. Tian, N. Chui, R. Lian, Q. Yang, W. Wang, C. Yang, D. Rao, J. Huang, Y. Zhang, F. Lai, C. Liu and T. Liu, *Energy Storage Mater.*, 2020, **27**, 591–598.

16 J. Zhang, P. Cui, Y. Gu, D. Wu, S. Tao, B. Qian, W. Chu and L. Song, *Adv. Mater. Interfaces*, 2019, **6**, 1901066.

17 D. M. Soares and G. Singh, *Nanotechnology*, 2020, **31**, 455406.

18 L. Yang, W. Hong, Y. Zhang, Y. Tian, X. Gao, Y. Zhu, G. Zou, H. Hou and X. Ji,

Adv. Funct. Mater., 2019, **29**, 1903454.

19 H. Huang, J. Cui, G. Liu, R. Bi and L. Zhang, *ACS Nano*, 2019, **13**, 3448–3456.

20 W. Wang, B. Jiang, C. Qian, F. Lv, J. Feng, J. Zhou, K. Wang, C. Yang, Y. Yang and S. Guo, *Adv. Mater.*, 2018, **30**, 1801812.

21 Q. Yu, B. Jiang, J. Hu, C. Y. Lao, Y. Gao, P. Li, Z. Liu, G. Suo, D. He, W. A. Wang and G. Yin, *Adv. Sci.*, 2018, **5**, 1800782.

22 Y. Wu, Y. Xu, Y. Li, P. Lyu, J. Wen, C. Zhang, M. Zhou, Y. Fang, H. Zhao, U. Kaiser and Y. Lei, *Nano Res.*, 2019, **12**, 2997–3002.

23 Q. Li, J. Peng, W. Zhang, L. Wang, Z. Liang, G. Wang, J. Wu, W. Fan, H. Li, J. Wang and S. Huang, *Adv. Energy Mater.*, 2023, 2300150.

24 Y. Wang, Z. Zhang, G. Wang, X. Yang, Y. Sui, F. Du and B. Zou, *Nanoscale Horiz.*, 2019, **4**, 1394–1401.

25 Y.-Z. Fang, R. Hu, K. Zhu, K. Ye, J. Yan, G. Wang and D. Cao, *Adv. Funct. Mater.*, 2020, **30**, 2005663.

26 L. Fan, K. Lin, J. Wang, R. Ma and B. Lu, *Adv. Mater.*, 2018, **30**, 1800804.

27 Y. Luo, L. Liu, K. Lei, J. Shi, G. Xu, F. Li and J. Chen, *Chem Sci*, 2019, **10**, 2048-2052.